Physics of Fluids

A Bayesian approach to the mean flow in a channel with small but arbitrarily directional system rotation

Cite as: Phys. Fluids **33**, 015103 (2021); https://doi.org/10.1063/5.0035552
Submitted: 29 October 2020 . Accepted: 10 December 2020 . Published Online: 06 January 2021

Xinyi L. D. Huang (黄馨仪), and Xiang I. A. Yang (杨翔)

A Bayesian approach to the mean flow in a channel with small but arbitrarily directional system rotation

Cite as: Phys. Fluids 33, 015103 (2021); doi: 10.1063/5.0035552
Submitted: 29 October 2020 • Accepted: 10 December 2020 •
Published Online: 6 January 2021

Xinyi L. D. Huang (黄馨仪) and Xiang I. A. Yang (杨翔)[a)]

AFFILIATIONS

Department of Mechanical Engineering, Pennsylvania State University, State College, Pennsylvania 16802, USA

[a)]Author to whom correspondence should be addressed: xzy48@psu.edu

ABSTRACT

The logarithmic law of the wall loses part of its predictive power in flows with system rotation. Previous work on the topic of mean flow scaling has mostly focused on flows with streamwise, spanwise, or wall-normal system rotation. The main objective of this work is to establish the mean flow scaling for wall-bounded flows with small but arbitrarily directional system rotation. Our approach is as follows. First, we apply dimensional analysis to the Reynolds-averaged momentum equation. We show that when a boundary-layer flow is subjected to small system rotation, the constant stress layer survives, and the mean flow U^+ is a universal function of y^+, Ω_x^+, Ω_y^+, and Ω_z^+, where U is the mean flow, y is the distance from the wall, Ω_i is the system rotation speed in the ith direction (in the locally defined coordinate), and the superscript + denotes normalization by the local wall units. Second, we survey the three-dimensional parameter space of $\Omega_{x,y,z}^+$ and determine $U^+(y^+, \Omega_x^+, \Omega_y^+, \Omega_z^+)$ for small Ω^+. Here, we conduct direct numerical simulation (DNS) of a $Re_\tau = 180$ channel at various rotation conditions. This approach is conventionally considered as "brutal force." However, as we will show in this work, the Bayesian approach allows us to very efficiently sample the parameter space. Four independent surveys are conducted with 146 DNSs, and the resulting Bayesian surrogate agrees well with our DNSs. Finally, we upscale to high Reynolds numbers via wall-modeled large-eddy simulation. In general, the present framework provides a path for surrogate modeling in a high-dimensional parameter space at high Reynolds numbers when sampling in a designated parameter space is possible at only a few conditions and at a low Reynolds number.

I. INTRODUCTION

Determining the behavior of an objective function within a designated parameter space is at the center of many engineering problems, and when an analytical approach is not possible (or too difficult), one often has to rely on "brutal force" parameter space surveys. A well-known example is the survey of the Reynolds number, a one-dimensional parameter space, for the mean flow scaling in a periodic plane channel.[1–6] In this work, we attempt to determine the mean flow scaling for wall-bounded flows with small but arbitrarily directional system rotation.

Flow with system rotation is encountered in, e.g., geophysics and turbomachinery. An extensively studied model problem of flow with system rotation is the rotating channel. Figure 1 is a sketch of the flow. Here, x denotes the local streamwise direction, y denotes the local wall-normal direction, and z denotes the local spanwise direction. The flow in Fig. 1 is controlled by four non-dimensional parameters, i.e., the Reynolds number, $Re_\tau = hu_{\tau,g}/\nu$; the streamwise rotation, $Ro_{\tau,x,g} = 2\Omega_x h/u_{\tau,g}$; the wall-normal rotation, $Ro_{\tau,y,g} = 2\Omega_y h/u_{\tau,g}$; and the spanwise rotation, $Ro_{\tau,z,g} = 2\Omega_z h/u_{\tau,g}$, where $\Omega = (\Omega_x, \Omega_y, \Omega_z)$ is the system rotation vector, h is the half channel height, $u_{\tau,g} = \sqrt{1/\rho \, dP/dx \, h}$ is the friction velocity, and the subscript g denotes a globally defined quantity (as opposed to a quantity defined for the flow near one of the two walls). $U = (U_x, U_y, U_z)$ is the mean velocity vector with U_x, U_y, U_z being the mean velocity in the streamwise, wall-normal, and spanwise directions. Limiting the system rotation in one of the three (global) Cartesian directions, many have conducted numerical simulations and laboratory experiments of streamwise, wall-normal, and spanwise rotating channels at both high and low rotation numbers.[7–16] For reasons that will be clear in Sec. II, we consider small Ω if $|\Omega \times U(y_t)| < u_{\tau,g}^2/h$. Here, $U(y_t)$ is the velocity at y_t, and y_t is the upper bound of the

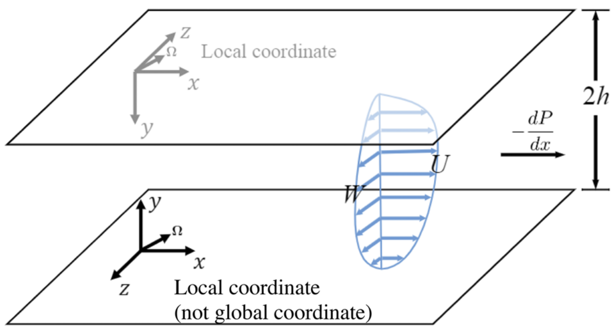

FIG. 1. A sketch of a channel with system rotation. The mean flow is not necessarily unidirectional nor symmetric with respect to the center plane. We define a local coordinate where x is the local streamwise direction, y is the wall-normal direction (pointing from the wall to the fluid), and z is the spanwise direction.

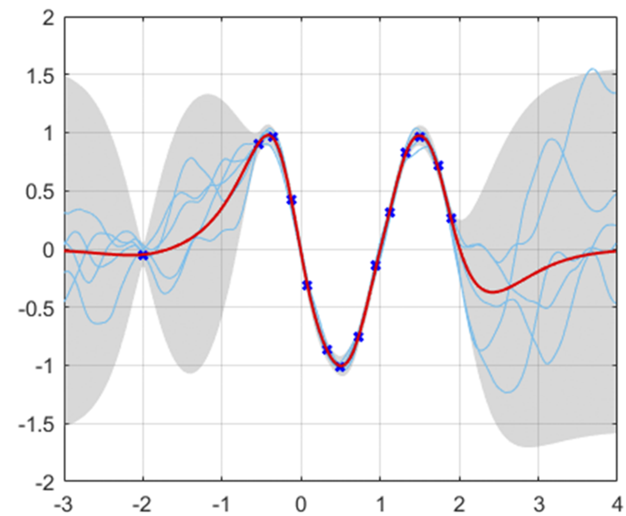

FIG. 2. Schematic of GPR. The symbols represent data, constraining the Gaussian process at the data locations. The thin lines are realizations of the Gaussian process. 95% of these realizations lie within the shaded region. Their mean gives the solid line, which is the estimate of the objective function. Parameters of the Gaussian process, e.g., the co-variances, are estimated from the data and are updated as more data become available. Further details of GPR could be found in Ref. 30.

logarithmic layer in an otherwise non-rotating channel. For flows at Reynolds number O(1000), the above requirement translates to $Ro_\tau \lesssim O(0.1)$. In the following, we briefly review previous discussion about mean flow's scaling in a channel with small system rotation. We will limit the discussion to the wall layer. The studies by Johnston *et al.*,[17] Yang *et al.*,[18] and a few others[16] concern with mean flow's scaling in the outer region at high rotation speeds and therefore fall out of the scope of this discussion. Flow with spanwise rotation seems to have received the most attention. By making an analogy between streamline curvature and buoyancy, Bradshaw[19] argued that a good approximation of the mean flow is $U = u_\tau/\kappa(\log(y^+) + \text{Constant}) + 2\beta\Omega y$ when subjected to small spanwise system rotation. Here, κ is the von Karman constant. The "constant" β is about 2 on the pressure side and 4 on the suction side, leading to an unphysical discontinuity at $\Omega = 0$. In his paper, Bradshaw did not argue for mean flow universality. Nakabayashi and Kitoh[20] resorted to dimensional analysis and concluded that the mean velocity at a distance y is only a function of y^+, $Rc = \Omega\nu/u_\tau^2$, and Re_τ when subjected to small spanwise system rotation. The authors argued that the logarithmic law of the wall survives, but the von Karman "constant" and the additive "constant" must depend on Re_τ and Rc. Here, allowing a Re_τ dependence defeats universality. Nickels and Joubert[21] compiled wind tunnel data and proposed $U^+ = L(y^+) + f_3(y^+)\Omega_z^+$, where $L(y^+)$ represents mean flow's scaling in a non-rotating channel and $f_3(y^+) = 9.7(y^+ - 35)$. This scaling is a first-order Taylor expansion around $\Omega_z = 0$. The scaling of Nickels and Joubert supports mean flow universality, but as we will show in Sec. III, keeping only the leading order term in the Taylor expansion is inadequate. Discussion of mean flow's scaling in a streamwise rotating channel and wall-normal rotation channel for small system rotation is difficult to find in the literature. To the best of our knowledge, the discussion does not go beyond the general arguments in Refs. 9 and 19.

There is little discussion about mean flow's scaling in flow with arbitrarily directional system rotation. In the absence of a good theory, responses of the mean flow to system rotation could only be obtained from a parameter space survey; see, e.g., Refs. 22–25 (for a partial survey of the parameter space). A naive "brutal force" approach is to sample the parameter space evenly. If one samples, e.g., 10 points in one dimension, a three-dimensional parameter space will require 10^3 samples, which would be nearly impossible if one were to use high-fidelity tools such as direct numerical simulation (DNS). To establish the mean flow scaling for flow subjected small but arbitrarily directional system rotation, we must resort to more efficient sampling strategies. In the following, we review a few candidates.[26] Following convention, we refer to a survey strategy as a "design."[26] Commonly used designs include the following: first, space-filling designs,[27] where one samples as sparsely as possible; second, Latin hypercube sampling, where one generates a near-random sample of parameter values to ensure that the target range in each dimension is sufficiently represented by the sample;[28] and third, entropy-based designs, where one maximizes the entropy of the sampling points in the parameter space.[29] These designs are agnostic to the objective function and therefore are less efficient than objective-function-aware methods. In this work, we resort the objective-function-aware method of Gaussian process regression (GPR) and Bayesian optimization.[30,31] GPR approximates objective functions as Gaussian processes. As a result, GPR does not only give an estimate of the objective function but also an uncertainty level of that estimate, as sketched in Fig. 2. The estimate of the objective function and the uncertainty of that estimate can be subsequently utilized for efficient sampling. For example, by sampling at the location with the largest uncertainty, one can quickly get a reliable estimate of the objective function. Other applications of GPR in turbulence research could be found in Refs. 32 and 33 and are not discussed here for brevity.

We briefly explain how we go about sampling the parameter space. For the discussion here, let us suppose we want to find out the behavior of U^+ (the objective function) in the parameter space of y^+, Ω_x^+, Ω_y^+, and Ω_z^+. Given an (initial) dataset, we will first build a Bayesian surrogate for the objective function. The Bayesian surrogate gives an estimate of the objective function in the designated parameter space as well as an estimate of the uncertainty level. The survey is based on an "acquisition function" whose maximum defines the next sampling location. For this study, the sampling strategy is a fully "explorative" one,[31] and the "acquisition function" is the "variance." From one "generation" to the next, parameters (or hyperparameters) of the underlying Gaussian process are updated according to the maximum likelihood. (We will explain "acquisition function," "explorative," "variance," and "generation" in Sec. III.) In order to save wall-clock time, instead of sampling at one location, we sample up to four locations simultaneously in one generation. Parallel sampling is, by itself, a research topic. In this work, we adopt the penalizing method.[34]

The rest of this paper is organized as follows: A dimensional analysis of the Reynolds-averaged momentum equation is presented in Sec. II, and we show mean flow universality in flow with small system rotation. The details and the results of the parameter space survey are presented in Sec. III. In Sec. IV, we show how to upscale from a low Reynolds number to a high Reynolds number. Finally, we conclude in Sec. V.

II. DIMENSIONAL ANALYSIS

Flow physics plays an important role in turbulence modeling even when taking a data-based approach. In order to safely generalize conclusions from one set of data to another, one must resort to physics or physical arguments. For example, DNS data of channel flow at $Re_\tau = 180$ itself does not provide insight into flow's behavior at $Re_\tau = 1000$, but knowing that U^+ is a universal function of y^+ for $y \ll h$,[35] we can use data at $Re_\tau = 180$ to infer the behavior of U^+ at $Re_\tau = 1000$ at least for small y^+ values, e.g., $y^+ < 36$. Here, 36 corresponds to $0.2h$ for the $Re_\tau = 180$ channel, below which the flow dynamics is not significantly affected by the outer length scale. In this section, we discuss the relevant flow physics.

A. Mean flow universality

We consider flow subjected to small but arbitrarily directional system rotation. Without loss of generality, let us consider a fully developed rotating channel subjected to system rotation of Ω in an arbitrary direction. (Here, "fully developed" means the velocity derivative with respect to x and z is 0.) The Reynolds-averaged Navier–Stokes equations can be written as

$$\frac{\partial\langle u_i' v'\rangle}{\partial y} = -\frac{1}{\rho}\frac{\partial\langle p\rangle}{\partial x_i} + \nu\frac{d^2 U_i}{dy^2} - \varepsilon_{ijk}\Omega_j U_k, \tag{1}$$

where $U_2 = 0$ because of the continuity equation, the mean convection in the wall-normal direction vanishes because $U_2 = 0$, the mean convection and the mean diffusion in the streamwise and spanwise directions vanish because the channel is fully developed, the turbulent transport in the streamwise and spanwise directions vanishes for the same reason, and the unsteady term vanishes because of Reynolds averaging. Integrating Eq. (1) from the wall to a distance y leads to

$$-\langle u_i' v'\rangle + \left[-\frac{1}{\rho}\frac{\partial\langle p\rangle}{\partial x_i}\right]y + \nu\frac{dU_i}{dy} + \left[-\varepsilon_{ijk}\Omega_j\right]\int_0^y U_k dy = \tau_w. \tag{2}$$

In the absence of system rotation, Eq. (2) reduces to

$$-\langle u' v'\rangle + \left[-\frac{1}{\rho}\frac{\partial\langle p\rangle}{\partial x}\right]y + \nu\frac{dU}{dy} = \tau_w. \tag{3}$$

For a y such that $y/\delta \ll 1$ and $1 \ll y^+$, i.e., for a y in the logarithmic layer, one can neglect the $O(y)$ term and the viscous term, and Eq. (3) gives rise to a constant stress layer, i.e.,

$$-\langle u' v'\rangle \approx \tau_w = u_\tau^2. \tag{4}$$

In this constant stress layer, the outer length scale is not relevant, and the mean flow U is a universal function of y, ν, and u_τ. Since we can get only one non-dimensional parameter from y, ν, and u_τ, i.e., yu_τ/ν, the PI theorem dictates that $U = u_\tau f(yu_\tau/\nu)$ for $y \ll \delta$ and $1 \ll y^+$. The above argument is still valid if we require $y/\delta \ll 1$ (and give up $1 \ll y^+$), in which case the viscous term cannot be neglected, and Eq. (3) becomes

$$-\langle u' v'\rangle + \nu\frac{dU}{dy} \approx \tau_w = u_\tau^2. \tag{5}$$

Again, the outer length scale is irrelevant, and U is a universal function of y, ν, and u_τ. The above discussion is very standard and can be found in, e.g., Ref. 35.

For flow with system rotation, the Coriolis term is

$$\lim_{y\to 0}\frac{\left[-\varepsilon_{ijk}\Omega_j\right]\int_0^y U_k dy}{y} = \lim_{y\to 0}\left[-\varepsilon_{ijk}\Omega_j\right]U_k = 0, \tag{6}$$

i.e., a high order term. In Eq. (6), we have invoked L'Hospital's rule[36] for the first equality and the no-slip condition at the wall for the second equality and assumed $\varepsilon_{ijk}\Omega_j^+ = O(1)$. It follows directly from Eq. (6) that the constant stress layer survives in a flow with small system rotation, and more importantly, at $y/\delta \ll 1$, $1 \ll y^+$, the mean velocity U is a universal function of y, u_τ, ν, $\Omega_{x,y,z}$. We can get four non-dimensional numbers from y, u_τ, ν, $\Omega_{x,y,z}$ (6 variables and 2 dimensions), i.e., y^+ and $\Omega_{x,y,z}^+$, and therefore, the PI theorem dictates

$$U^+ = f\left(y^+, \Omega_{x,y,z}^+\right), \tag{7}$$

where the superscript + denotes normalization by the local wall units. In Eq. (7), the non-dimensional number $\Omega_{x,y,z}^+$ is a combination of the rotation number and the Reynolds number,

$$\Omega_{x,y,z}^+ = \frac{h\Omega_{x,y,z}}{u_\tau}\frac{\nu}{u_\tau h} = \frac{Ro_{\tau,x,y,z}}{2Re_\tau}. \tag{8}$$

Similar to flow in a non-rotating channel, if we require $y \ll \delta$ (and give up $1 \ll y^+$), Eq. (7) is valid in both the constant stress layer and the viscous layer. A direct result of the above discussion is that one can use data at a low Reynolds number to infer mean flow's behavior at a high Reynolds number as long as $Ro_{\tau,x,y,z}/Re_\tau$ are the same. This effectively reduces the dimension of the parameter space from four, i.e., Re_τ, $Ro_{\tau,x,y,z}$ to three, i.e., $\Omega_{x,y,z}^+$.

B. A few considerations

First, we remark on the mean flow three dimensionality. By neglecting the Coriolis term and the pressure gradient term in the constant stress layer, the Reynolds-averaged Navier–Stokes equation reduces to

$$-\langle u_i' v'\rangle + \nu\frac{dU_i}{dy} \approx \tau_{w,i}, \tag{9}$$

where i = 1, 3. It follows from the above equation that mean flow three dimensionality, which is an important flow feature outside the constant stress layer, is not an issue in and below the constant stress layer. Hence, if one wants an equilibrium-type of wall model, wall modeling for boundary-layer flows with small system rotation does not need to account for mean flow three dimensionality [as long as the large-eddy simulation (LES)/wall-modeling matching location is within the constant stress layer, and one defines the local coordinate to align the x axis with the local flow].

Second, we define "small" system rotation. It follows from Eq. (6) that "small" system rotation requires a Coriolis term < pressure gradient term, i.e.,

$$\varepsilon_{ijk}\Omega_j \int_0^y U_k dy < \frac{1}{\rho}\frac{\partial P}{\partial x_i} y. \tag{10}$$

A sufficient condition of the above inequality is

$$\varepsilon_{ijk}\Omega_j U_k < \frac{1}{\rho}\frac{\partial P}{\partial x_i}. \tag{11}$$

Requiring the above inequality to hold in the constant stress layer is to require $|\Omega \times U| < u_\tau^2/h$. In practice, the following range of rotation speed seems to be sufficiently small for a flow at $Re_\tau = 180$: $-1 \le Ro_{\tau,x,g} \le 1$, $-0.01 \le Ro_{\tau,y,g} \le 0.01$, $-1 \le Ro_{\tau,z,g} \le 1$.

III. PARAMETER SPACE SURVEY

A. Details of the Gaussian process regression and the acquisition function

GPR predicts a mean and a variance at an unsampled location in the parameter space. The mean is the estimate of the objective function at that unsampled location, and the variance measures the uncertainty of GPR's estimate. Specifically, given input/output data pairs $(\mathbf{x}_1, \mathbf{z}_1)$ $(\mathbf{x}_2, \mathbf{z}_2)$, . . ., $(\mathbf{x}_n, \mathbf{z}_n)$, the mean, and the variance at an unsampled location $\mathbf{x}_*$ are[30]

$$M(\mathbf{x}_*) = k(\mathbf{x}_*, \mathbf{X})\left(k(\mathbf{X},\mathbf{X}) + \sigma^2 I\right)^{-1}\mathbf{z}, \tag{12}$$

$$\Sigma(\mathbf{x}_*) = k(\mathbf{x}_*, \mathbf{x}_*) + \sigma^2 I - k(\mathbf{x}_*, \mathbf{X})\left(k(\mathbf{X},\mathbf{X}) + \sigma^2 I\right)^{-1} k(\mathbf{X}, \mathbf{x}_*), \tag{13}$$

where M is the mean, Σ is the variance, $\mathbf{X} = (\mathbf{x}_1, \mathbf{x}_2, \ldots, \mathbf{x}_n)$, $\mathbf{z} = (\mathbf{z}_1, \mathbf{z}_2, \ldots, \mathbf{z}_n)$, $k(\mathbf{x}_1, \mathbf{x}_2)$ is the covariance matrix, I is the identity matrix, and σ is a measure of data uncertainty. For the present study, we use the Matern 5/2 kernel.[30] The parameters in the kernel are determined according to maximum likelihood. For this specific application, the objective function is $\mathbf{z} = U^+ - [1/\kappa \log(y^+) + B]$, where $\kappa = 0.41$ is the von Karman constant, $B = 5.2$ is the additive constant, and the input is $\mathbf{x} = (y^+, 2\Omega_x^+, 2\Omega_y^+, 2\Omega_z^+)$.

To know where to sample next, one must define an "acquisition function," $\alpha(\mathbf{x})$, the maximum of which gives the next sampling location. Here, we define the acquisition function as follows:

$$\alpha = \int_{y^+=10}^{y^+=60} \Sigma |dM|, \tag{14}$$

which measures the uncertainty of the mean M. The integration limits are at $y^+ = 10$ and $y^+ = 60$, precluding the viscous layer and the non-universal outer layer. The integration variable is $dM = dM/dy\, dy$ instead of dy to give more weight to regions where M changes rapidly. The acquisition function α is only a function of Ω^+. In the case of parallel sampling, the maximum of the acquisition function α gives the first sampling location, i.e., $\bar{\mathbf{x}}_1$, and the maximum of the following penalized acquisition function α_2 gives the second sampling location,

$$\alpha_2 = \alpha\phi, \ \phi = 1 - k_n(\bar{\mathbf{x}}_1, \bar{\mathbf{x}}), \tag{15}$$

where ϕ is the penalizer and k_n is the normalized Matern 5/2 kernel. Repeating this process n times yields to $n + 1$ sampling points. For the present study, we limit the number of parallel sampling to 4.

B. Details of the direct numerical simulations

We solve the incompressible Navier–Stokes equation in a rectangular domain, as sketched in Fig. 3,

$$\frac{\partial u_i}{\partial t} + u_j \frac{\partial u_i}{\partial x_j} = -\frac{1}{\rho}\frac{\partial p}{\partial x_i} + \nu \frac{\partial^2 u_i}{\partial x_j \partial x_j} - \varepsilon_{ijk} 2\Omega_j u_k, \tag{16}$$

$$\frac{\partial u_i}{\partial x_i} = 0, \tag{17}$$

where i = 1, 2, 3 are the streamwise, wall-normal, and spanwise directions, u_i is the instantaneous velocity along the ith coordinate, $\rho \equiv 1$ is the density (which will be dropped hereon for brevity), and ε_{ijk} is the Levi-Civita symbol. Our code uses a spectral method in all three Cartesian directions with explicit time stepping. Further details of the code can be found in Ref. 10. The size of the computational domain is $L_x \times L_y \times L_z = 4\pi \times 2 \times 2\pi$, which is four times the size of a minimum channel.[4] Although strong system rotation, e.g., strong streamwise rotation, leads to elongated streamwise rollers that require a much larger computational domain,[12] weak system rotation, as considered in this work, does not give rise to such structures; see Fig. 4.

The grid size is $N_x \times N_y \times N_z = 192 \times 120 \times 180$. The resolutions are $\Delta x^+ \approx 12$ in the streamwise direction, $\Delta z^+ \approx 6$ in the spanwise direction, and $\Delta y^+ \approx 5$ at the channel centerline, which is comparable to (if not finer than) the resolution of previous studies.[1,9] The flow is driven by a constant pressure gradient in the streamwise direction, and we apply a no-slip boundary condition on both walls. All calculations are initialized with a random velocity field. Flow statistics are averages for about 40 flow throughs after the flow reaches a statistically stationary state, where one flow through is L_x/u_b.

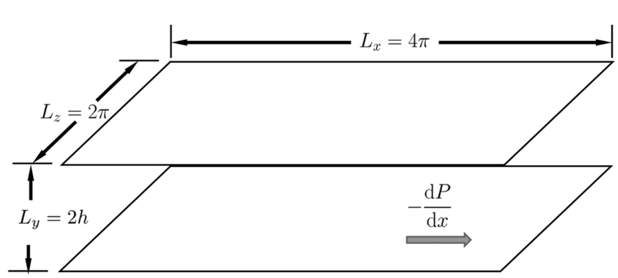

FIG. 3. A sketch of the computational domain. Here, the half channel height $h \equiv 1$ and will be dropped hereon for brevity.

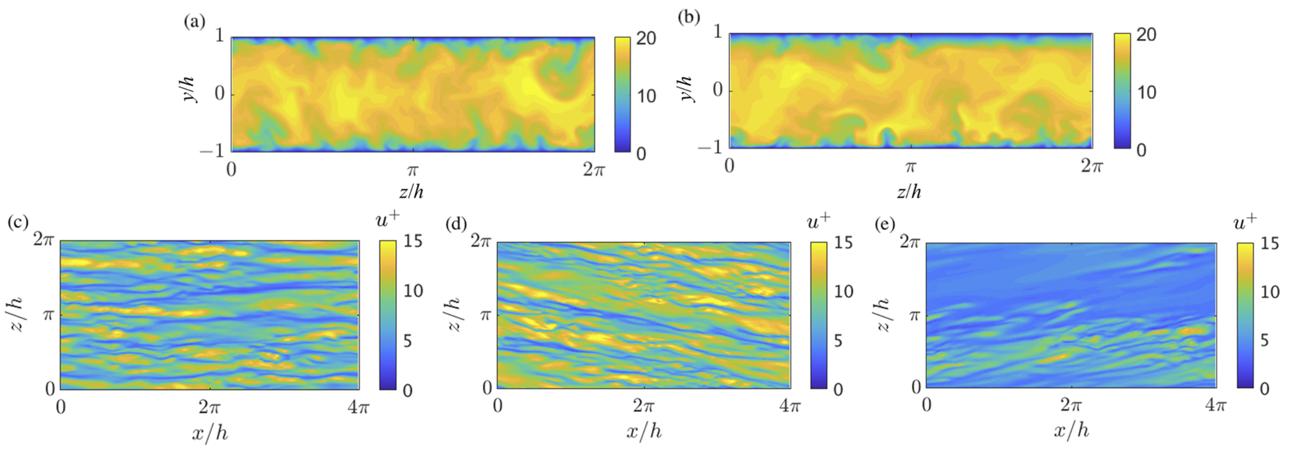

FIG. 4. The instantaneous streamwise velocity at a constant x location in (a) a non-rotating channel and (b) a rotating channel with $Ro_{\tau,x,g}$ = 1.0, $Ro_{\tau,y,g}$ = 0.01, $Ro_{\tau,z,g}$ = 1.0, and the instantaneous streamwise velocity at a constant y location in (c) a non-rotating channel and [(d) and (e)] a rotating channel with $Ro_{\tau,x,g}$ = 1.0, $Ro_{\tau,y,g}$ = 0.01, $Ro_{\tau,z,g}$ = 1.0. (d) and (e) are at a distance 0.05h from the two wall. (d) is near the bottom wall, and (e) is near the top wall. Spanwise rotation leads to a pressure side and a suction side, where the turbulence is augmented near the pressure side, i.e., in (d), and suppressed near the suction side, i.e., in (e).

Figure 5 shows a sample time history of the flow rate for 300 flow throughs in one of our DNSs.

DNSs resolve all turbulent scales, and therefore, statistical convergence is the main source of uncertainty. In order to estimate the uncertainty due to the lack of statistical convergence, we repeat the same DNS (but with different random initial conditions) nine times (at the flow condition $Ro_{\tau,x,g} = 1$, $Ro_{\tau,y,g} = 0.01$, $Ro_{\tau,z,g} = 1$). Figure 6 shows the resulting nine profiles. We measure the data uncertainty according to

$$\sigma = \frac{1}{60-10}\int_{y^+=10}^{y^+=60} \mathrm{STD}(U^+(y))dy^+ \approx 0.15, \tag{18}$$

leading to an uncertainty of about $0.15u_\tau$. Here, STD(·) is the standard deviation of the quantity in the parentheses.

C. Details of the parameter space surveys

We carry out four independent parameter space surveys. Table I summarizes the details of the four surveys. We refer to these four surveys as S1, S2, S3, and S4. 146 DNSs are conducted. S1, S2, and S3 differ in terms of N_p and the number of parallel sampling. S3 and S4 differ in terms of the initial dataset size N_0. We use two initial datasets: one contains eight datasets at the eight corners of the parameter space and the other contains 27 data points at $\bar{\mathbf{x}} = (0 + 1\,i, 0 + 0.01\,j, 0 + 1\,k)$ with i, j, k = −1, 0, and 1. Under rotation, even small, the flow in general becomes asymmetric about the channel center plane. Hence, each DNS will lead to two sampling points in the parameter space of $Ro_{\tau,x/y/z,g}$.

The objective functions are $U^+ = \sqrt{U_1^2 + U_3^2}$. The target parameter space is $-1/180 \le Ro_{\tau,x}/Re_\tau \le 1/180$, $-0.01/180 \le Ro_{\tau,y}/Re_\tau \le 0.01/180$, and $-1/180 \le Ro_{\tau,z}/Re_\tau \le 1/180$ (in addition to $10 < y^+ < 60$). Because the flow is not symmetric with respect to the channel center plane, the target parameter space does not exactly correspond to $-1 < Ro_{\tau,x,g} < 1$, $-0.01 < Ro_{\tau,y,g} < 0.01$, $-1 < Ro_{\tau,z,g} < 1$. We can get a rough idea of mean flow's variation in the parameter space by plotting U^+ at the eight corners of the parameter space. Figure 7 shows the eight velocity profiles. We see that mean flow's response to system rotation is non-negligible and non-trivial, justifying a parameter space survey.

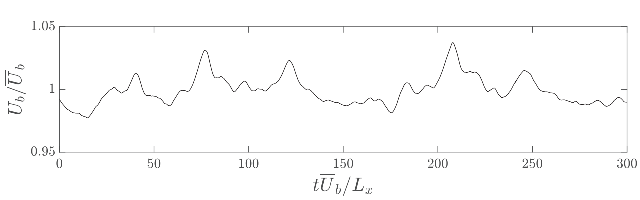

FIG. 5. A sample time history of the instantaneous flow rate over 300 flow throughs.

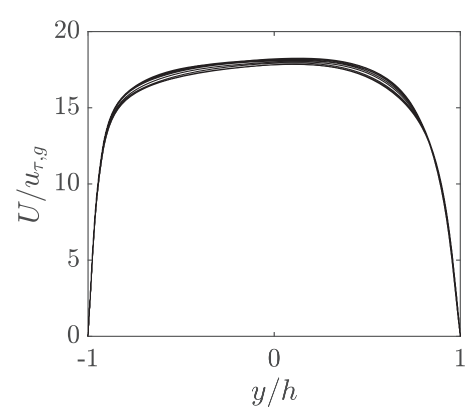

FIG. 6. Nine profiles obtained by repeating the same DNS nine times at the same flow condition $Ro_{\tau,x,g}$ = 1, $Ro_{\tau,y,g}$ = 0.01, $Ro_{\tau,z,g}$ = 1 but with different random initialization.

TABLE I. Details of the four parameter space surveys. N_0 is the size of the initial dataset. N_p is the number of parallel sampling points. N_g is the number of generations. N_t is the total number of DNSs in the survey. 146 DNSs are conducted: 1 per generation × 18 generations +2 × 12 + 4 × 9 + 4 × 9 + 27 + (9 — 1) — 3, where 27 is the initial dataset size. 9 — 1 DNSs are conducted to estimate the uncertainty due to statistical convergence, and —3 is because S1's and S2's first generation is a subset of S3's first generation.

	N_0	N_p	N_g	N_t
S1	27	1	18	45
S2	27	2	12	51
S3	27	4	9	63
S4	8	4	9	44

Before we proceed to the results, we comment on the relationship between data and our interpretation of the data. Data in itself is independent from our interpretation. For example, given a parameter space, an accurate surrogate of $\mathbf{z}(\mathbf{x})$ will be an equally accurate surrogate of $\mathbf{z}'(\mathbf{x}')$, irrespective of the physical considerations behind the choice of $\mathbf{x}$ and $\mathbf{x}'$. Here, $\mathbf{z}' = f_1(\mathbf{z})$, $\mathbf{x}' = f_2(\mathbf{x})$. A physically inspired objective function answers questions that are not directly registered near the dataset, whereas an arbitrary defined objective function cannot generalize. For this study, we define the objective function as $U^+ = U/u_\tau$ because the analysis in Sec. II suggests that U^+ is universal.

D. Results

Each survey leads to a set of data points in the parameter space and a Bayesian surrogate of U^+ as a function of y^+, Ω_x^+, Ω_y^+, and Ω_z^+. Figure 8 shows the query points projected on the $Ro_{\tau,x,g}$-$Ro_{\tau,y,g}$ plane, the $Ro_{\tau,x,g}$-$Ro_{\tau,z,g}$ plane, and the $Ro_{\tau,y,g}$-$Ro_{\tau,z,g}$ plane. The query points that belong to the same "generation" are separated owing to the use of a penalizer. Overall, the data appear to be "randomly" scattered in the parameter space, and the searching path does not seem to reveal any inner structure of the parameter space.

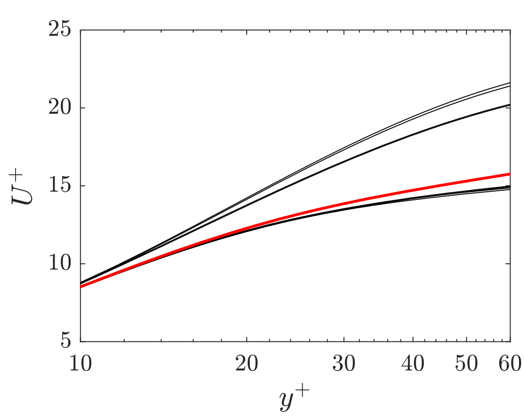

FIG. 7. Mean velocity profiles at the eight corners of the target parameter space (thin black lines) and in a non-rotating channel (red line). The purpose of this figure is to show the range of mean flow's variation in the target parameter space, and therefore, the correspondence between each black line and the flow condition (in terms of system rotation) is not important.

Figure 9 compares the Bayesian surrogate (before sampling) and the DNS at the sampling location, i.e., at SM-g$N.n$, for M = 1, 2, 3; N = 2, 4, 6; and n = 1. Here, SM-g$N.n$ is the sampling point of survey SM, generation N, and query point n. Per our definition of the acquisition function, the sampling location is where the GPR is the least reliable. Hence, the figure, to some extent, measures the convergence of the survey at SM-g$N.n$. We make the following observations. Given a SM, the surrogate converges to DNS as a function of gN, as can be seen by comparing (a), (b), and (c); (d), (e), and (f); (g), (h), and (i); and (j), (k), and (l). Given a gN and an initial dataset, the estimate is more accurate if we do more parallel sampling, as can be seen by comparing (a), (d), and (g); (b), (e), and (h); and (c), (f), and (i). Given a gN and the number of parallel sampling, a larger initial dataset leads to a more accurate estimate, as can be seen by comparing (g) and (j), (h) and (k), and (i) and (l). Figure 10 compares the Bayesian surrogate (before sampling) and the DNS at the sampling location SM-g$N{\cdot}n$ such that there is the same number of sampled points in the parameter space. For example, for S1-g5.1, there are 27 + 4 × 1 = 31 sampled points within the parameter space; for S2-g3.1, there are 27 + 2 × 2 = 31 sampled points in the parameter space; and for S4-g6.4, there are 8 + 5 × 4 + 3 = 31 sampled points in the parameter space (3 are due to parallel sampling). We make the following observations. Given the number of sampled points and an initial dataset, the estimate is less reliable if one does more parallel sampling, as can be seen by comparing (a), (d), and (g); (b), (e), and (h); and (c), (f), and (i). Given the number of sampled points and the parallel sampling strategy, the estimate is more reliable if the initial dataset is smaller, as can be seen by comparing (g) and (j), and (h) and (k). These results provide best practices for Bayesian-based parameter space surveys. The general conclusion is that sampling, according to a Bayesian approach, leads to more efficient use of resources.

Next, we examine the convergence of the four surveys. Knowing the exact solution of U^+ in the parameter space is difficult. However, a good estimation of the exact solution, $M_{\rm all}$, could be obtained by building a surrogate using all of our 146 DNSs. The convergence of a specific survey could be measured according to

$$\mathrm{err} = \left[\frac{1}{\Delta y^+}\int_{y^+=10}^{y^+=60} \left|M(y^+,\bar{\mathbf{x}}^*) - M_{\rm all}(y^+,\bar{\mathbf{x}}^*)\right|^2 dy^+\right]^{1/2}, \tag{19}$$

where $\Delta y^+ = 60 - 10 = 50$ and $\bar{\mathbf{x}}^*$ is where the estimated uncertainty Σ takes the maximum. Figures 11(a) and 11(b) show err as a function of generation and dataset size for S1, S2, S3, and S4. Surveys S1, S2, and S3 have the same initial dataset and therefore the same initial err. S4 has a smaller initial dataset and therefore a larger initial err. All surveys converge quickly: within a few generations, err is about 0.1, which is comparable to the uncertainty of the DNS data (which is 0.15). (Obviously, the surrogate can be considered as converged when its error is smaller than the uncertainty in DNS.)

The accuracy of a particular surrogate model, e.g., S3, could also be directly examined by comparing its predictions to DNSs. Figure 12 compares S3 surrogate's predictions at eight locations where DNS data are available and the uncertainties are the largest. As shown in Fig. 12, the Bayesian surrogate follows the DNS very

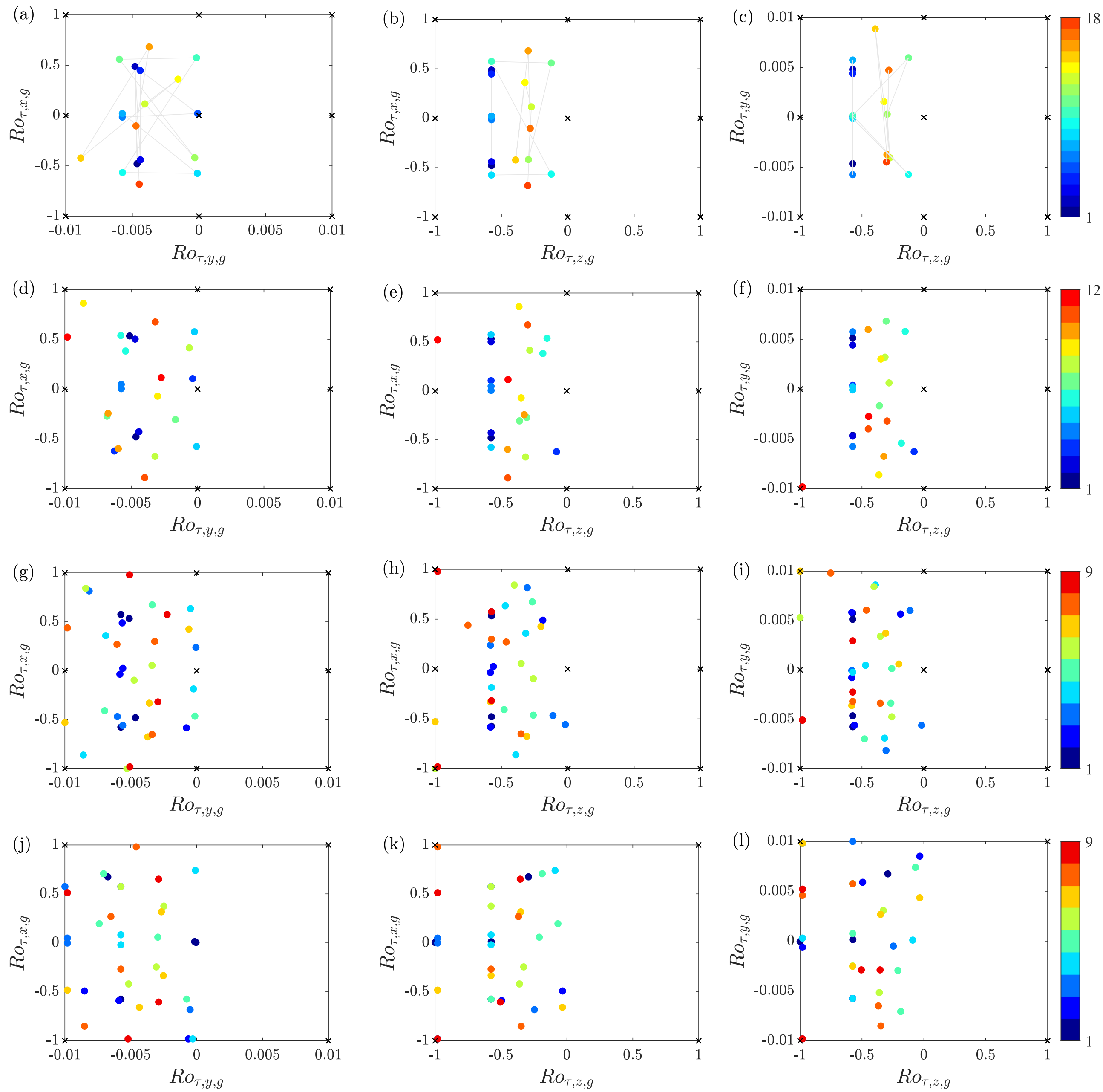

FIG. 8. The query points projected on [(a), (d), (g), and (j)] the $Ro_{\tau,y,g}$-$Ro_{\tau,x,g}$ plane, [(b), (e), (h), and (k)] the $Ro_{\tau,z,g}$-$Ro_{\tau,x,g}$ plane, and [(c), (f), (i), and (l)] the $Ro_{\tau,z,g}$-$Ro_{\tau,y,g}$ plane. [(a), (b), and (c)] S1. [(d), (e), and (f)] S2. [(g), (h), and (i)] S3. [(j), (k), and (l)] S4. Computing one channel subjected to system rotation of $Ro_{\tau,x,g}$, $Ro_{\tau,y,g}$, $Ro_{\tau,z,g}$ adds two data points to the parameter space: the flow near the bottom wall represents a data point at $Ro_{\tau,x,g}$, $Ro_{\tau,y,g}$, $Ro_{\tau,z,g}$, and the flow near the top wall represents a data point at $Ro_{\tau,x,g}$, -$Ro_{\tau,y,g}$, -$Ro_{\tau,z,g}$. Here, we plot only query points in the left two quadrants. Cross symbols represent the initial dataset. Generations are color coded. For S1, we query one point every time. This allows us to visualize a querying path, as shown in (a), (b), and (c).

closely. The results of S1, S2, and S4 are similar and are not shown here for brevity.

E. Further analytical analysis

In this subsection, we estimate the behavior of U^+ analytically. The objective is to compare the data-based approach and the analytical approach. We follow the same steps that give rise to the logarithmic law of the wall. That is, we first arrive at a physically sound form and then determine the unknowns from data. In the case of the logarithmic law of the wall, the constant stress layer assumption and the mixing length model give rise to the logarithmic form, where the unknown coefficients, i.e., the

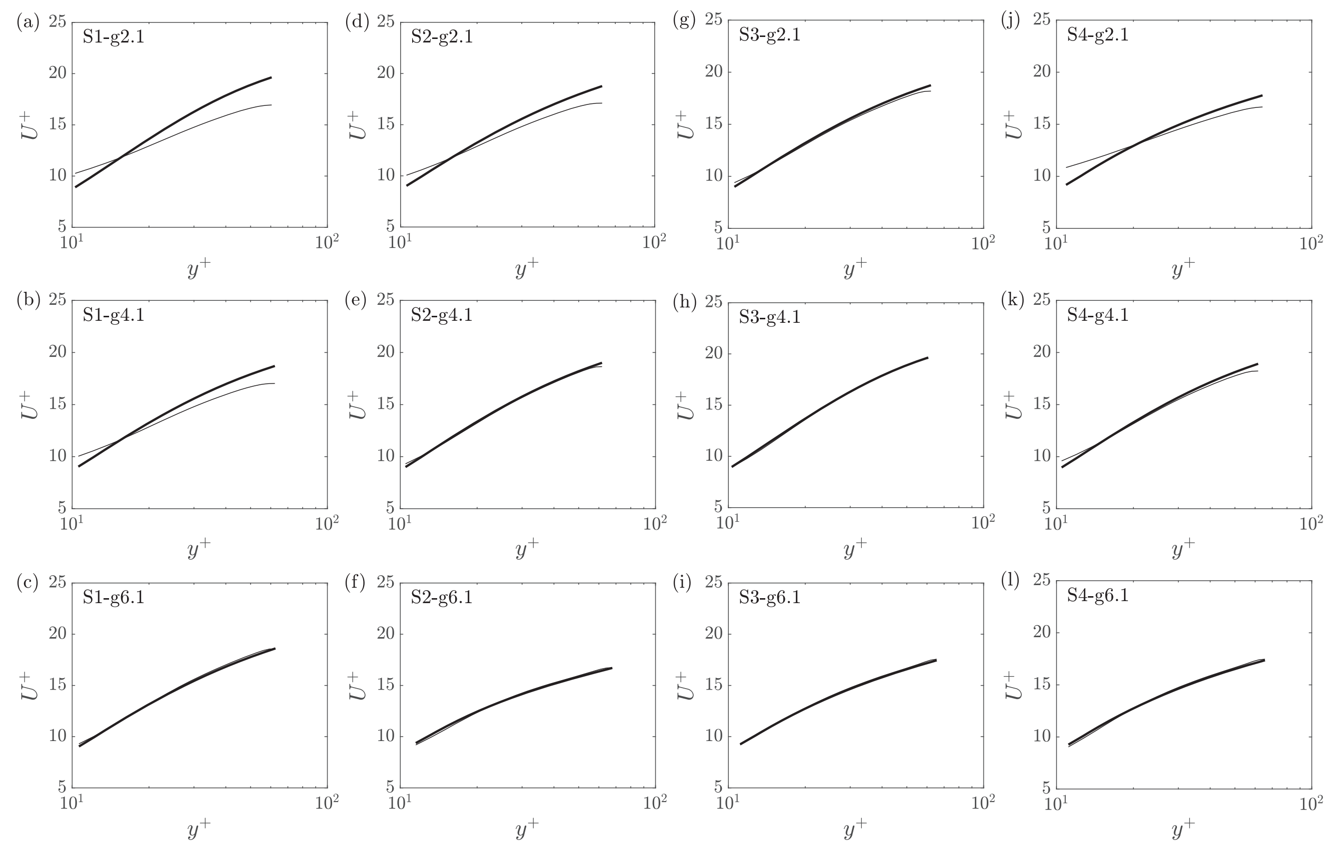

FIG. 9. A comparison of the GPR estimate (before sampling) and the DNS for [(a), (b), and (c)] S1, [(d), (e), (f)] S2, [(g), (h), and (i)] S3, [(j), (k), and (l)] S4. [(a), (d), (g), and (j)] Generation 2. [(b), (e), (h), and (k)] Generation 4. [(c), (f), (i), and (l)] Generation 6. The bold lines are DNS, and the thin lines are GPR.

von Karman constant κ and the addend B, are determined from data.

Firs, in order to get a physically sound form, we apply the Taylor expansion to Eq. (7) at $\Omega^+_{x,y,z} = 0$. This gives

$$U^+ = L(y^+) + F + S + H, \tag{20}$$

where $L(y^+)$ is the conventional law of the wall containing the viscous sublayer, the buffer layer, and the logarithmic layer; F contains the first-order terms,

$$F = f_1\Omega^+_x + f_2\Omega^+_y + f_3\Omega^+_z; \tag{21}$$

S contains the second order terms,

$$S = s_1\Omega^{+2}_x + s_2\Omega^{+2}_y + s_3\Omega^{+2}_z + s_4\Omega^+_x\Omega^+_y + s_5\Omega^+_y\Omega^+_z + s_6\Omega^+_x\Omega^+_z; \tag{22}$$

and H contains the higher order terms. Here, $f_1, f_2, f_3, s_1, s_2, s_3, s_4, s_5, s_6$ are functions of y^+. f_1 and f_2 can be determined from symmetric considerations. First, because $U^+(y^+, \Omega^+_x, \Omega^+_y = 0, \Omega^+_z = 0) = U^+(y^+, -\Omega^+_x, \Omega^+_y = 0, \Omega^+_z = 0)$, we conclude that $f_1 = 0$. Second, because $U^+(y^+, \Omega^+_x = 0, \Omega^+_y, \Omega^+_z = 0) = U^+(y^+, \Omega^+_x = 0, -\Omega^+_y, \Omega^+_z = 0)$, we conclude that $f_2 = 0$. Keeping the leading order terms, we have

$$U^+ = L(y^+) + f_3\Omega^+_z + s_1\Omega^{+2}_x + s_2\Omega^{+2}_y + s_4\Omega^+_x\Omega^+_y, \tag{23}$$

where, again, f_3, s_1, s_2, and s_4 are functions of y^+ and can be obtained from data,

$$\begin{aligned}
f_3(y^+) &= \frac{U^+(y^+, \Omega^+_x = 0, \Omega^+_y = 0, \Omega^+_z) - L(y^+)}{\Omega^+_z},\\
s_1(y^+) &= \frac{U^+(y^+, \Omega^+_x, \Omega^+_y = 0, \Omega^+_z = 0) - L(y^+)}{\Omega^{+2}_x},\\
s_2(y^+) &= \frac{U^+(y^+, \Omega^+_x = 0, \Omega^+_y, \Omega^+_z = 0) - L(y^+)}{\Omega^{+2}_y},\\
s_4(y^+) &= \frac{U^+(y^+, \Omega^+_x, \Omega^+_y, \Omega^+_z = 0) - L(y^+) - s_1(y^+)\Omega^{+2}_x - s_2(y^+)\Omega^{+2}_y}{\Omega^+_x\Omega^+_y}.
\end{aligned} \tag{24}$$

Measuring f_3 in a DNS with $Ro_{\tau,z,g} = 1$, measuring s_1 in a DNS with $Ro_{\tau,x,g} = 1$, measuring s_2 in a DNS with $Ro_{\tau,y,g} = 0.01$, and measuring s_4 in a DNS with $Ro_{\tau,x,g} = 1$, $Ro_{\tau,y,g} = 0.01$, we plot the f_3, s_1, s_2, and s_4 in Fig. 13.

Compared to a parameter space survey, the advantage of an analytical approach is that it requires fewer samples/calculations. For example, Eq. (23) contains four unknowns, which are fully determined by four calculations. Nonetheless, we could also make use of all 146 DNSs to fit for f_3, s_1, s_2, and s_4. In that case, the objective is to find $f_3(y^+)$, $s_1(y^+)$, $s_2(y^+)$, and $s_4(y^+)$ such that $f_3\Omega_z + s_1\Omega_x^2 + s_2\Omega_y^2$

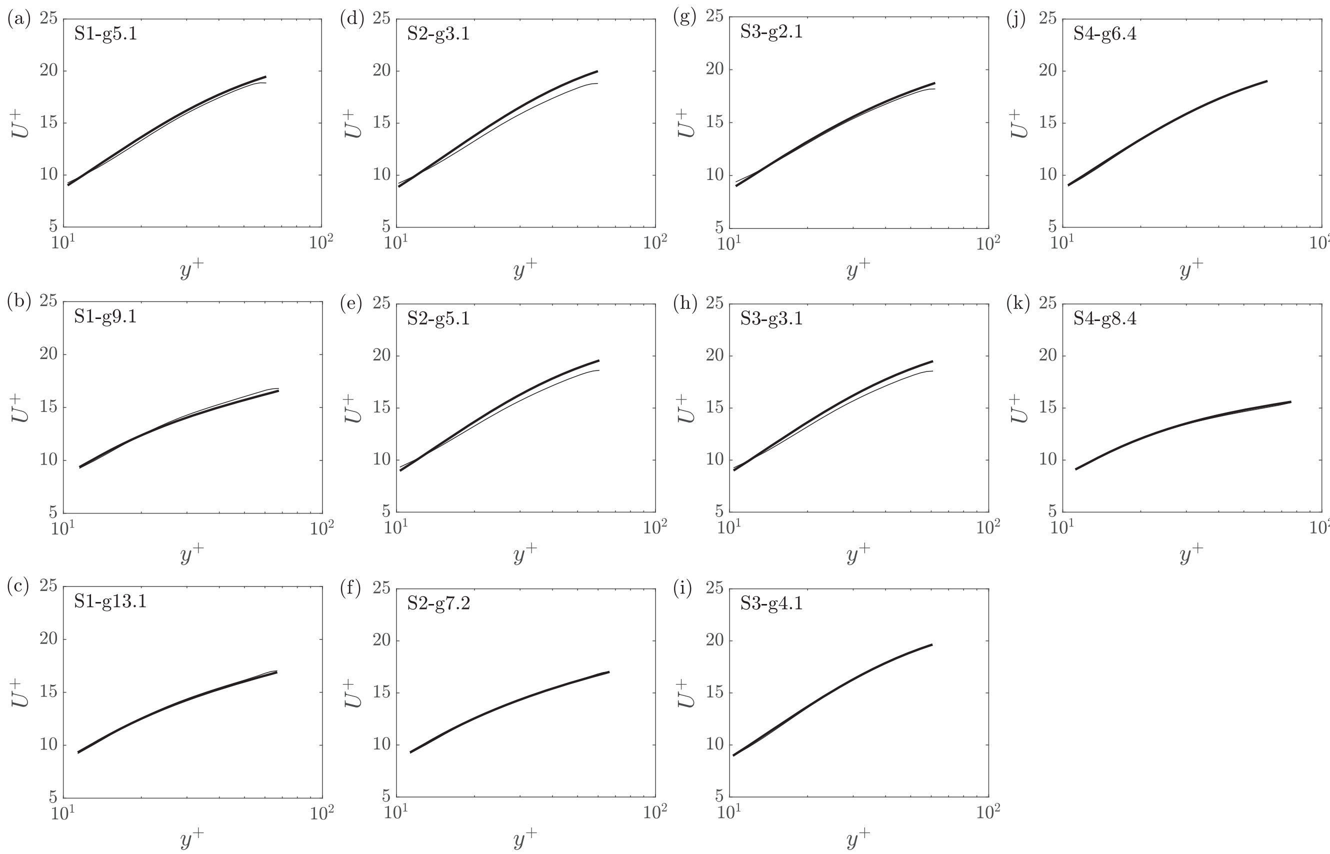

FIG. 10. A comparison of the GPR estimate (before sampling) and the DNS for [(a), (b), and (c)] S1, [(d), (e), and (f)] S2, [(g), (h), and (i)] S3, and [(j) and (k)] S4. The bold lines are DNS data, and the thin lines are GPR estimates.

$+ s_4\Omega_x\Omega_y$ is as close to $U^+ - L(y^+)$ as possible. In another word, the objective is to find f_3, s_1, s_2, and s_4 such that

$$\min_{f_3,s_1,s_2,s_4} \left(U^+ - L^+ - f_3\Omega_z^+ - s_1\Omega_x^{+2} - s_2\Omega_y^{+2} - s_4\Omega_x^+\Omega_y^+\right)^2 \tag{25}$$

for all possible Ω_x, Ω_y, and Ω_z in the parameter space. This is a linear regression problem. Figure 14 shows the results. Now, if Eq. (23) is the truth, f_3, s_1, s_2, and s_4 obtained according to Eqs. (24) and (25) should be the same. However, comparing Figs. 13 and 14, we see that Eqs. (24) and (25) lead to different f_3, s_1, s_2, and s_4. As such, we can already conclude that Eq. (23) is not a good approximation of the mean flow in the surveyed parameter space.

In Fig. 15, we compare the S3 surrogate and Eq. (23) at two $\bar{\mathbf{x}}$ locations. The Gaussian regression surrogate agrees with DNS at both conditions. The analytical model [Eq. (23)] with f_3, s_1, s_2, and s_4 obtained according to Eq. (24) captures the trend; Eq. (23) with f_3, s_1, s_2, and s_4 obtained according to (25) is comparably more accurate. While one may argue that more involved math[9] could potentially

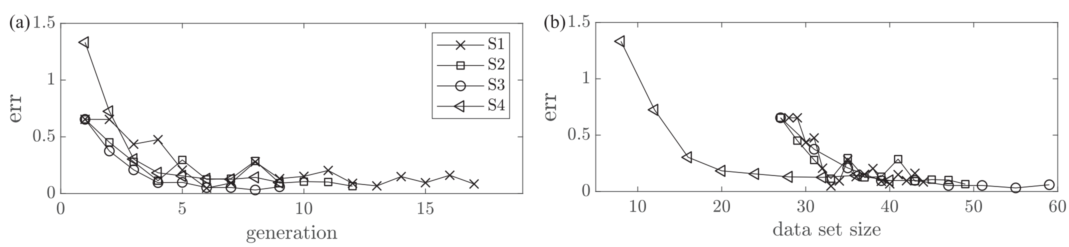

FIG. 11. (a) err as a function of generation. (b) err as a function of dataset size. The spent resource is measured by the dataset size.

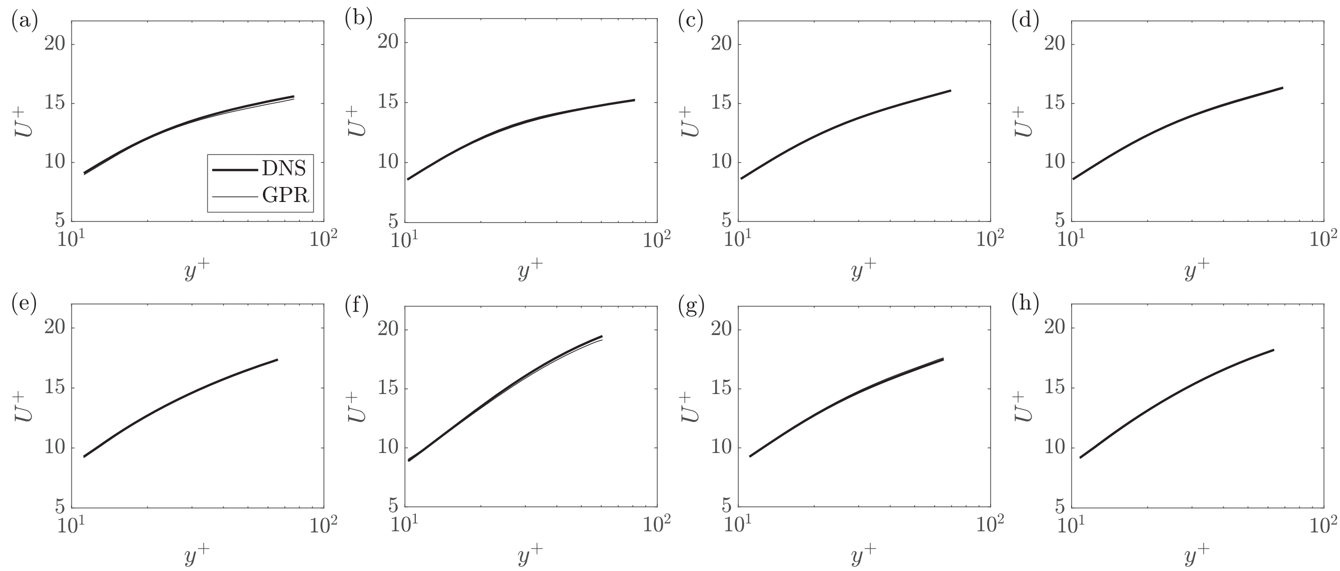

FIG. 12. Predictions of the S3 surrogate at locations in the parameter space where DNS data are available and the uncertainty of the surrogate is the largest. DNS of flow at these conditions belong to S1, S2, and S4, not S3, and therefore, labeling these cases as in Fig. 10 would not be very informative.

lead to more accurate analytical estimates of $U^+(y^+, \Omega^+_{x,y,z})$, the same thing could be said about GPR: non-linear Bayesian method and more advanced sampling strategy[37] could also give more accurate estimates. In all, the results suggest that the data-based method is more accurate than the analytical method.

IV. UPSCALE

In Sec. II, we conclude that the mean flow in the constant stress layer is a universal function of y^+, $\Omega^+_{x,y,z}$. Taking a data-based approach, in Sec. III, we determine U^+ as a function of $\Omega^+_{x,y,z}$ for

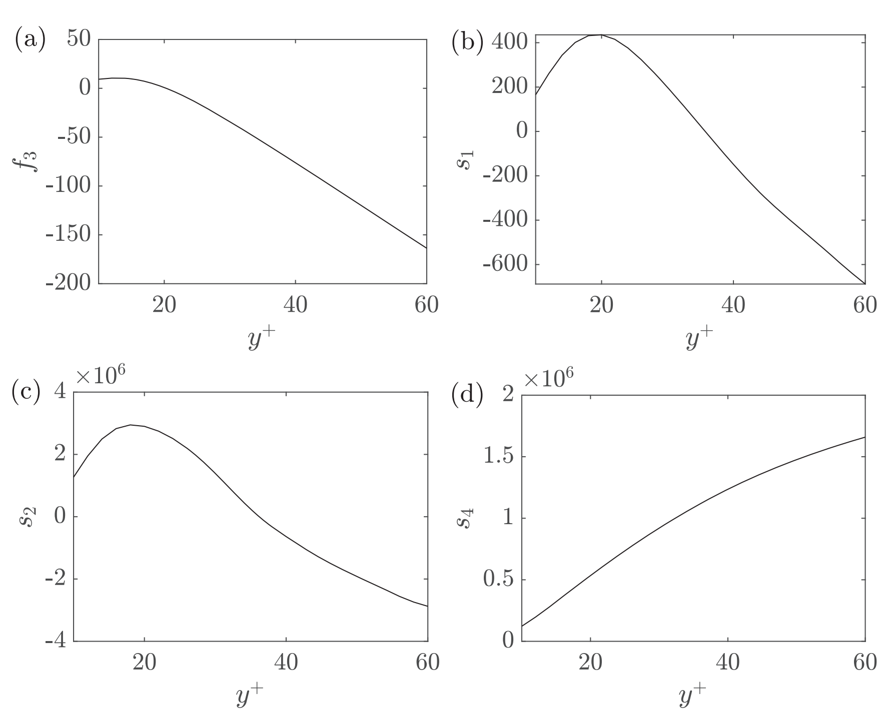

FIG. 13. (a) f_3, (b) s_1, (c) s_2, and (d) s_4 obtained according to Eq. (24). Normalization is by the local wall units.

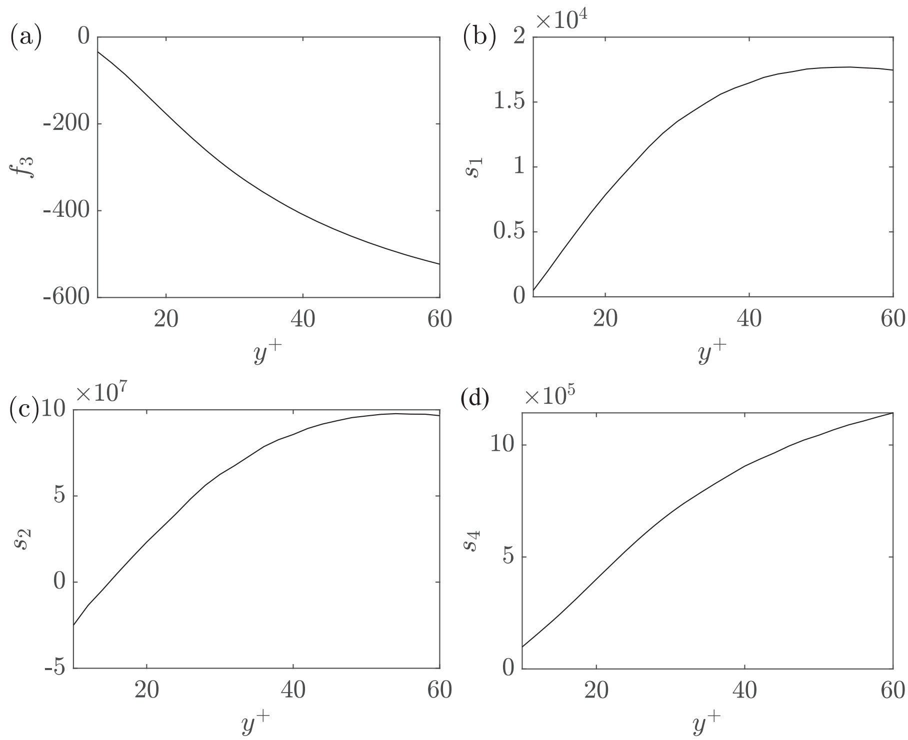

FIG. 14. (a) f_3, (b) s_1, (c) s_2, and (d) s_4 obtained according to Eq. (25). Normalization is by the local wall units.

$y^+ < 60$. However, real-world applications that involve system rotation are at very high Reynolds numbers,[38–41] and the knowledge of the flow for $y^+ < 60$ is not going to be very useful. In this subsection, we discuss how one may determine the mean flow for $y^+ > 60$ without resorting to DNS.

For illustration purposes, consider channel flow with no system rotation. Say, we know that U^+ is a universal function of y^+ but not the functional dependence. Let us also suppose that we now have knowledge of $U^+(y^+)$ for $y^+ < 60$. To determine $U^+(y^+)$ for $y^+ > 60$ without resorting to DNS, we resort to wall-modeled large-eddy simulation (WMLES). Specifically, we can conduct a WMLES at the Reynolds number $Re_\tau = 1920$, for which we will use 64 grid points in the wall-normal direction. The first off-wall grid point of the WMLES will be at $y^+ = 1920/(64/2) = 60$, where we know $U(y^+)$. The constant stress layer extends to about $y/\delta = 0.2$, and therefore, the $Re_\tau = 1920$ WMLES gives knowledge of the mean flow up to $y^+ = 384$. Repeating this process two times will give $U^+(y^+)$ for $y^+ < 2500$ and four times will give $U^+(y^+)$ for $y^+ < 10^5$. For channel flow without system rotation, this process will trivially lead to the logarithmic law of the wall. By applying the same procedure to a rotating channel, we will be able to gain knowledge of $U^+(y^+)$ for y^+ of practical relevance.

To verify this approach, we conduct WMLES at the condition $Re_{\tau,g} = 976$, $Ro_{\tau,g} = 3.1$. DNS data of flow at this condition

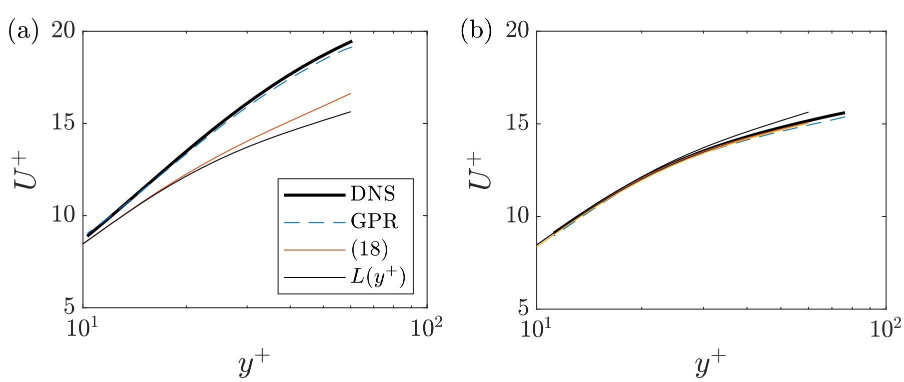

FIG. 15. $U^+(y^+)$ for (a) $\Omega_x^+ = -0.0043$, $\Omega_y^+ = -4.31\times10^{-5}$, $\Omega_z^+ = -0.0043$ and (b) $\Omega_x^+ = -0.0040$, $\Omega_y^+ = 4.03 \times 10^{-5}$, $\Omega_z^+ = 0.0016$. We plot DNS, Bayesian surrogate, Eq. (23), and the conventional law of the wall $L(y^+)$.

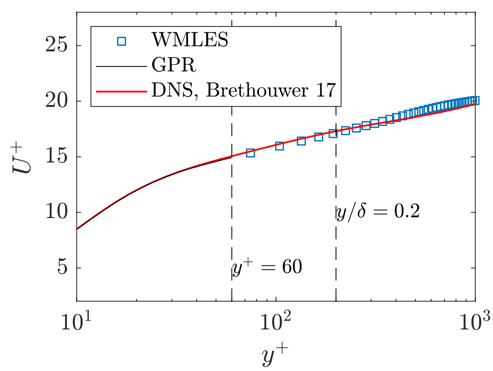

FIG. 16. WMLES results where the Bayesian surrogate is used as a wall model. The flow is at the condition $Re_{\tau,g}$ = 976, $Ro_{\tau,g}$ = 3.1. Here, GPR is "Gaussian process regression." DNS is from Ref. 11.

are available in Ref. 11. We use the in-house pseudo-spectral code LESGO for our WMLES. Details of the code could be found in Refs. 42 and 43 and the references cited therein. We use 32 grid points in the wall normal direction. The LES/wall model matching location is at h^+_{wm} = 55, i.e., 10 < h^+_{wm} < 60. Figure 16 shows the results. We make a few observations. First, GPR obtained from $Re_{\tau,g}$ = 180 agrees well with the DNS at $Re_{\tau,g}$ = 976, providing further support to mean flow universality. Second, WMLES agrees well with the DNS within the constant stress layer, i.e., 60 < y^+, y/δ < 0.2, providing support to the proposed upscaling approach.

To further demonstrate this approach, we carry out WMLES of channel flow at $Re_\tau = 3000$ for $\Omega_x^+ = 3.33 \times 10^{-4}$, $\Omega_y^+ = 3.33 \times 10^{-6}$, $\Omega_z^+ = 3.33 \times 10^{-4}$. (Note that the relevant parameters are $\Omega^+_{x,y,z}$, not Ro_τ.) The first off-wall grid point is at h^+_{wm} = 47 (10 < h^+_{wm} < 60). Figure 17 shows the results. With this WMLES, we now have knowledge of $U^+(y^+, \Omega_x^+ = 3.33 \times 10^{-4}, \Omega_y^+ = 3.33 \times 10^{-6}, \Omega_z^+ = 3.33 \times 10^{-4})$ for $y^+ \lesssim 0.2 \times 3000 = 600$. Surveying the entire three-dimensional parameter space of $\Omega^+_{x,y,z}$ with WMLES gives the U^+ behavior for $y^+ > 60$, and the results are not shown here for brevity.

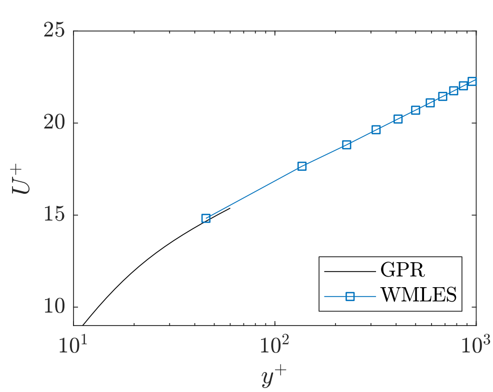

FIG. 17. WMLES results where the Bayesian surrogate is used as a wall model.

V. CONCLUSIONS

This work presents a framework for surrogate modeling in a high-dimensional flow controlling parameter space and at high Reynolds numbers, when an analytical approach is too difficult and sampling of the parameter space is possible at only a few conditions and at low Reynolds numbers. We establish the mean flow scaling in a channel subjected to small but arbitrarily directional system rotation. We show, for the first time, the existence of a constant stress layer in wall-bounded flows with small system rotation. According to our dimensional analysis, the Reynolds-averaged momentum equation in the horizontal directions reduces to Eq. (9) for $y \ll \delta$. We draw two conclusions from Eq. (9). First, mean flow three dimensionality is not an important issue in the constant stress layer—in fact, given strong mean flow three dimensionality, the momentum flux at the top of the constant stress layer and wall-shear stress would be in two very different directions, and there would not be a constant stress layer to begin with. As a result, if one needs an equilibrium-type wall model for flow with small system rotation, he/she can follow the conventional approach and model for the velocity magnitude. Second, mean flow, when normalized using the local friction velocity, is a universal function of y^+ and $\Omega^+_{x,y,z}$. We then determine mean flow's behavior as a function of y^+, Ω_x^+, Ω_y^+, and Ω_z^+ by sampling the parameter space of Ω^+ following a Bayesian approach. The Bayesian surrogate converges to the truth very quickly within O(10) iterations. In comparison, if one evenly samples the three-dimensional parameter, 10 points in each dimension would already require 10^3 calculations. The resulting Bayesian surrogate describes the behavior of $U^+(y^+, \Omega_x^+, \Omega_y^+, \Omega_z^+)$ for $-5.5 \times 10^{-3} < 2\Omega_x^+ < 5.5 \times 10^{-3}$, $-5.5\times10^{-5} < 2\Omega_y^+ < 5.5\times10^{-5}$, $-5.5\times10^{-3} < 2\Omega_z^+ < 5.5\times10^{-3}$ and for $y^+ < 60$ (for small y^+). Here, the relevant parameter is Ω^+ not Ro_τ according to our dimensional analysis. Finally, we upscale to high Reynolds numbers by coupling WMLES and DNS. Here, a half channel is used for our WMLES. Employing a half channel is a common practice for geophysical flow calculations where Earth's rotation is an important consideration.[44] The end result is the knowledge of the mean flow in a rotating channel with small system rotation in any arbitrary direction. It is worth noting that although the same framework can be used to determine mean flow's behavior at high rotational speeds, the resulting scaling would not be universal because mean flow universality breaks at high rotational speeds.

ACKNOWLEDGMENTS

X.I.A.Y. thanks ONR (Grant No. N000142012315) for financial support. X.I.A.Y. thanks Dr. G. Brethouwer (2017) for providing the DNS data. X.I.A.Y. thanks Dr. M. Abkar for providing useful comments. Part of the DNSs were performed on the XSEDE.

APPENDIX: THE SAMPLED LOCATIONS

In this appendix, we tabulate all the sampled locations in the parameter space (Tables II–V).

TABLE II. A list of query points in S1.

Gen	$Ro_{\tau,x,g} \times 1$	$Ro_{\tau,y,g} \times 100$	$Ro_{\tau,z,g} \times 1$	Gen	$Ro_{\tau,x,g} \times 1$	$Ro_{\tau,y,g} \times 100$	$Ro_{\tau,z,g} \times 1$	Gen	$Ro_{\tau,y,g} \times 100$	$Ro_{\tau,z,g} \times 1$	$Ro_{\tau,z,g} \times 1$
1	−0.48	−0.46	−0.58	7	0.02	0.58	−0.58	13	0.12	−0.41	−0.28
2	0.49	0.48	−0.58	8	−0.58	−0.01	−0.58	14	0.36	0.16	−0.32
3	−0.44	0.44	−0.58	9	−0.57	−0.57	−0.12	15	−0.42	0.89	−0.39
4	0.45	0.44	−0.58	10	0.58	0.02	−0.58	16	0.68	−0.37	−0.30
5	0.02	0.01	−0.58	11	0.56	0.60	−0.12	17	−0.10	0.47	−0.28
6	−0.02	−0.58	−0.58	12	−0.42	0.03	−0.30	18	−0.69	0.45	0.30

TABLE III. A list of query points in S2.

Gen	$Ro_{\tau,x,g} \times 1$	$Ro_{\tau,y,g} \times 100$	$Ro_{\tau,z,g} \times 1$	Gen	$Ro_{\tau,x,g} \times 1$	$Ro_{\tau,y,g} \times 100$	$Ro_{\tau,z,g} \times 1$	Gen	$Ro_{\tau,y,g} \times 100$	$Ro_{\tau,z,g} \times 1$	$Ro_{\tau,z,g} \times 1$
1a	−0.48	−0.46	−0.58	5a	−0.58	−0.01	−0.58	9a	−0.07	0.3	−0.35
1b	0.53	0.51	−0.58	5b	0.58	0.02	−0.58	9b	0.86	0.86	0.36
2a	−0.43	0.44	−0.58	6a	0.54	0.58	−0.15	10a	−0.24	−0.67	−0.32
2b	0.50	−0.47	−0.58	6b	0.38	−0.54	−0.18	10b	−0.60	0.60	−0.45
3a	0.11	0.04	−0.58	7a	−0.31	−0.17	−0.36	11a	0.67	−0.32	−0.30
3b	−0.62	−0.63	−0.08	7b	−0.27	0.68	−0.30	11b	−0.89	0.40	0.45
4a	0.00	−0.58	−0.58	8a	0.41	0.06	−0.28	12a	0.12	−0.27	−0.45
4b	0.05	0.58	−0.58	8b	−0.67	0.32	−0.31	12b	0.52	0.98	0.98

TABLE IV. A list of query points in S3.

Gen	$Ro_{\tau,x,g} \times 1$	$Ro_{\tau,y,g} \times 100$	$Ro_{\tau,z,g} \times 1$	Gen	$Ro_{\tau,x,g} \times 1$	$Ro_{\tau,y,g} \times 100$	$Ro_{\tau,z,g} \times 1$	Gen	$Ro_{\tau,y,g} \times 100$	$Ro_{\tau,z,g} \times 1$	$Ro_{\tau,z,g} \times 1$
1a	−0.48	−0.46	−0.58	4a	−0.19	−0.03	−0.58	7a	−0.33	−0.36	−0.58
1b	0.53	0.51	−0.58	4b	0.64	0.05	−0.47	7b	0.43	0.06	−0.20
1c	−0.58	0.58	−0.58	4c	−0.86	−0.86	0.39	7c	−0.53	−1.00	1.00
1d	0.58	−0.58	−0.58	4d	0.36	−0.69	−0.32	7d	−0.67	0.37	−0.31
2a	0.03	−0.56	−0.56	5a	−0.46	0.01	−0.26	8a	0.30	−0.32	−0.58
2b	−0.58	−0.08	−0.58	5b	0.67	−0.34	−0.27	8b	−0.65	−0.34	−0.35
2c	0.49	−0.56	0.19	5c	−0.41	−0.7	−0.48	8c	0.27	0.60	−0.46
2d	−0.03	0.58	−0.58	5d	0.55	0.01	1.03	8d	0.44	−0.98	0.75
3a	0.24	−0.01	−0.58	6a	0.06	0.34	−0.35	9a	−0.32	0.29	−0.58
3b	−0.56	−0.56	−0.02	6b	−0.10	−0.47	−0.26	9b	0.58	−0.22	−0.58
3c	−0.47	0.60	−0.11	6c	−1.00	−0.53	1.00	9c	0.98	0.51	0.98
3d	0.82	0.82	0.31	6d	0.84	−0.84	0.40	9d	−0.98	0.51	0.98

TABLE V. A list of query points in S4.

Gen	$Ro_{\tau,x,g} \times 1$	$Ro_{\tau,y,g} \times 100$	$Ro_{\tau,z,g} \times 1$	Gen	$Ro_{\tau,x,g} \times 1$	$Ro_{\tau,y,g} \times 100$	$Ro_{\tau,z,g} \times 1$	Gen	$Ro_{\tau,y,g} \times 100$	$Ro_{\tau,z,g} \times 1$	$Ro_{\tau,z,g} \times 1$
1a	0.01	0.02	−0.57	4a	0.08	0.58	−0.58	7a	0.32	0.27	−0.35
1b	0.00	0.00	1.00	4b	−0.02	−0.58	−0.58	7b	−0.66	0.43	−0.03
1c	−0.58	−0.58	−0.58	4c	−0.98	−0.03	0.98	7c	−0.33	−0.25	−0.58
1d	0.67	0.67	−0.29	4d	0.74	0.01	−0.09	7d	−0.48	−0.98	0.98
2a	−0.59	0.59	−0.49	5a	0.06	−0.29	−0.21	8a	−0.27	0.58	−0.58
2b	0.58	−0.58	−0.58	5b	0.20	0.74	−0.07	8b	0.27	−0.65	−0.37
2c	−0.49	−0.85	0.03	5c	−0.58	0.08	−0.58	8c	0.98	−0.46	0.98
2d	−0.98	0.06	0.98	5d	0.71	−0.71	−0.19	8d	−0.85	0.85	0.35
3a	−0.68	−0.05	−0.25	6a	−0.25	0.31	−0.33	9a	0.65	−0.29	−0.36
3b	0.58	1.00	−0.58	6b	0.58	0.58	−0.58	9b	−0.98	−0.52	0.98
3c	0.05	−0.98	0.98	6c	−0.42	−0.52	−0.36	9c	0.51	0.98	0.98
3d	−0.00	0.98	0.98	6d	0.38	−0.25	−0.58	9d	−0.60	−0.29	−0.51

DATA AVAILABILITY

The data that support the findings of this study are available from the corresponding author upon reasonable request.

REFERENCES

[1] J. Kim, P. Moin, and R. Moser, "Turbulence statistics in fully developed channel flow at low Reynolds number," J. Fluid Mech. **177**, 133–166 (1987).

[2] J. Graham, K. Kanov, X. I. A. Yang, M. Lee, N. Malaya, C. C. Lalescu, R. Burns, G. Eyink, A. Szalay, R. D. Moser *et al.*, "A web services accessible database of turbulent channel flow and its use for testing a new integral wall model for LES," J. Turbul. **17**(2), 181–215 (2016).

[3] S. Hoyas and J. Jiménez, "Scaling of the velocity fluctuations in turbulent channels up to $Re_\tau = 2003$," Phys. Fluids **18**(1), 011702 (2006).

[4] A. Lozano-Durán and J. Jiménez, "Effect of the computational domain on direct simulations of turbulent channels up to $Re_\tau = 4200$," Phys. Fluids **26**(1), 011702 (2014).

[5] M. Lee and R. D. Moser, "Direct numerical simulation of turbulent channel flow up to $Re_\tau \approx 5200$," J. Fluid Mech. **774**, 395–415 (2015).

[6] Y. Yamamoto and Y. Tsuji, "Numerical evidence of logarithmic regions in channel flow at $Re_\tau = 8000$," Phys. Rev. Fluids **3**(1), 012602 (2018).

[7] J. P. Johnson, "The effects of rotation on boundary layers in turbomachine rotors," in *Fluid Mechanics, Acoustics, and Design of Turbomachinery,* SP-304 Part 1, (NASA, 1974), pp. 207-249.

[8] R. Kristoffersen and H. I. Andersson, "Direct simulations of low-Reynolds-number turbulent flow in a rotating channel," J. Fluid Mech. **256**, 163–197 (1993).

[9] M. Oberlack, W. Cabot, B. A. P. Reif, and T. Weller, "Group analysis, direct numerical simulation and modelling of a turbulent channel flow with streamwise rotation," J. Fluid Mech. **562**, 383–403 (2006).

[10] Z. Xia, Y. Shi, and S. Chen, "Direct numerical simulation of turbulent channel flow with spanwise rotation," J. Fluid Mech. **788**, 42–56 (2016).

[11] G. Brethouwer, "Statistics and structure of spanwise rotating turbulent channel flow at moderate Reynolds numbers," J. Fluid Mech. **828**, 424–458 (2017).

[12] Z. Yang and B.-C. Wang, "Capturing Taylor-Görtler vortices in a streamwise-rotating channel at very high rotation numbers," J. Fluid Mech. **838**, 658–689 (2018).

[13] Y.-J. Dai, W.-X. Huang, and C.-X. Xu, "Coherent structures in streamwise rotating channel flow," Phys. Fluids **31**(2), 021204 (2019).

[14] C. Bergmann and B.-C. Wang, "Direct numerical simulation of turbulent heat transfer in a wall-normal rotating channel flow," Int. J. Heat Fluid Flow **80**, 108480 (2019).

[15] X. Yang, Z.-H. Xia, J. Lee, Y. Lv, and J. Yuan, "Mean flow scaling in a spanwise rotating channel," Phys. Rev. Fluids **5**(7), 074603 (2020).

[16] Z. Yang, B.-Q. Deng, B.-C. Wang, and L. Shen, "On the self-constraint mechanism of the cross-stream secondary flow in a streamwise-rotating channel," Phys. Fluids **32**(10), 105115 (2020).

[17] J. P. Johnston, R. M. Halleent, and D. K. Lezius, "Effects of spanwise rotation on the structure of two-dimensional fully developed turbulent channel flow," J. Fluid Mech. **56**(3), 533–557 (1972).

[18] X. I. A. Yang, Z.-H. Xia, J. Lee, Y. Lv, and J.-L. Yuan, "Mean flow scaling in a spanwise rotating channel," in *Center for Turbulence Research Annual Briefs* (Stanford University, 2018), pp. 285–297.

[19] P. Bradshaw, "The analogy between streamline curvature and buoyancy in turbulent shear flow," J. Fluid Mech. **36**(1), 177–191 (1969).

[20] K. Nakabayashi and O. Kitoh, "Low Reynolds number fully developed two-dimensional turbulent channel flow with system rotation," J. Fluid Mech. **315**, 1–29 (1996).

[21] T. B. Nickels and P. N. Joubert, "The mean velocity profile of turbulent boundary layers with system rotation," J. Fluid Mech. **408**, 323–345 (2000).

[22] H. Wu and N. Kasagi, "Effects of arbitrary directional system rotation on turbulent channel flow," Phys. Fluids **16**(4), 979–990 (2004).

[23] I. N. Esau, "The coriolis effect on coherent structures in planetary boundary layers," J. Turbul. **4**(1), 37–41 (2003).

[24] P. Pulkkinen, I. Tuominen, A. Brandenburg, A. Nordlund, and R. F. Stein, "Rotational effects on convection simulated at different latitudes," Astron. Astrophys. **267**, 265–274 (1993).

[25] L. M. Smith and F. Waleffe, "Transfer of energy to two-dimensional large scales in forced, rotating three-dimensional turbulence," Phys. Fluids **11**(6), 1608–1622 (1999).

[26] T. J. Santner, B. J. Williams, W. Notz, and B. J. Williams, *The Design and Analysis of Computer Experiments* (Springer, 2003), Vol. 1.

[27] L. Pronzato and W. G. Müller, "Design of computer experiments: Space filling and beyond," Stat. Comput. **22**(3), 681–701 (2012).

[28] J.-S. Park, "Optimal Latin-hypercube designs for computer experiments," J. Stat. Plan. Inference **39**(1), 95–111 (1994).

[29] R. Bettinger, P. Duchêne, L. Pronzato, and E. Thierry, "Design of experiments for response diversity," J. Phys.: Conf. Ser. **135**, 012017 (2008).

[30] C. E. Rasmussen and C. K. I. Williams, *Gaussian Processes for Machine Learning* (MIT Press, Cambridge, MA, 2006).

[31] S. Theodoridis, *Machine Learning: A Bayesian and Optimization Perspective* (Academic Press, 2015).

[32] C. Talnikar, P. Blonigan, J. Bodart, and Q. Wang, "Parallel optimization for LES," in *Proceedings of the Summer Program* (Center for Turbulence Research, Stanford University, 2014), p. 315.

[33] O. Mahfoze, A. Moody, A. Wynn, R. Whalley, and S. Laizet, "Reducing the skin-friction drag of a turbulent boundary-layer flow with low-amplitude wall-normal blowing within a Bayesian optimization framework," Phys. Rev. Fluids **4**(9), 094601 (2019).

[34] D. Ginsbourger, R. Le Riche, and L. Carraro, "Kriging is well-suited to parallelize optimization," in *Computational Intelligence in Expensive Optimization Problems* (Springer, 2010), pp. 131–162.

[35] S. B. Pope, *Turbulent Flows* (Cambridge University Press, 2001).

[36] G. Strang and E. P. Herman, *Calculus: Volume 1* (OpenStax, 2018).

[37] P. T. Roy, L. Jofre, J.-C. Jouhaud, and B. Cuenot, "Versatile sequential sampling algorithm using kernel density estimation," Eur. J. Oper. Res. **284**(1), 201–211 (2020).

[38] M. Barringer, A. Coward, K. Clark, K. A. Thole, J. Schmitz, J. Wagner, M. A. Alvin, P. Burke, and R. Dennis, "The design of a steady aero thermal research turbine (start) for studying secondary flow leakages and airfoil heat transfer," in *ASME Turbo Expo 2014: Turbine Technical Conference and Exposition* (American Society of Mechanical Engineers Digital Collection, 2014).

[39] J. Lee, G. Xia, G. Medic, and O. Sharma, "Impact of transverse shear on turbomachinery endwall flow," in Proceedings of the Summer Program, 2018.

[40] R. F. Kunz and B. Lakshminarayana, "Three-dimensional Navier–Stokes computation of turbomachinery flows using an explicit numerical procedure and a coupled k-ε turbulence model," J. Turbomach **114**(3), 627–642 (1992).

[41] R. B. Medvitz, R. F. Kunz, D. A. Boger, J. W. Lindau, A. M. Yocum, and L. L. Pauley, "Performance analysis of cavitating flow in centrifugal pumps using multiphase CFD," J. Fluids Eng. **124**(2), 377–383 (2002).

[42] E. Bou-Zeid, C. Meneveau, and M. Parlange, "A scale-dependent Lagrangian dynamic model for large eddy simulation of complex turbulent flows," Phys. Fluids **17**(2), 025105 (2005).

[43] X. L. Huang, X. I. Yang, and R. F. Kunz, "Wall-modeled large-eddy simulations of spanwise rotating turbulent channels—Comparing a physics-based approach and a data-based approach," Phys. Fluids **31**(12), 125105 (2019).

[44] R. Stoll, J. A. Gibbs, S. T. Salesky, W. Anderson, and M. Calaf, "Large-eddy simulation of the atmospheric boundary layer," Bound. Layer Meteorol. **177**(2), 541–581 (2020).